Journal of Sound and Vibration 325 (2009) 989–999

Contents lists available at ScienceDirect

Journal of Sound and Vibration

journal homepage: www.elsevier.com/locate/jsvi

Power transmission through a hollow cylinder by acoustic waves and piezoelectric transducers with radial polarization

C.F. Lü [a], J.S. Yang [b], J. Wang [c], W.Q. Chen [a,d,*]

[a] Department of Civil Engineering, Zhejiang University, Hangzhou 310058, PR China
[b] Department of Engineering Mechanics, University of Nebraska, Lincoln, NE 68588-0526, USA
[c] Mechanics and Materials Science Research Center, School of Engineering, Ningbo University, Ningbo 315211, PR China
[d] Department of Engineering Mechanics, Zhejiang University, Hangzhou 310027, PR China

ARTICLE INFO

Article history:
Received 1 December 2008
Received in revised form
30 March 2009
Accepted 3 April 2009
Handling Editor: L.G. Tham
Available online 7 May 2009

ABSTRACT

Transmission of electric energy through an elastic hollow cylinder by acoustic waves is investigated using the linear theories of piezoelectricity and elasticity. The elastic cylinder is between two perfectly bonded piezoelectric layers of piezoelectric ceramics with radial polarization. Power transmission is achieved through the electrical excitation of axisymmetric thickness-stretch vibrations. An exact solution is obtained which is validated by comparison with a solution from the state space method (SSM). Numerical results are presented for the transmitted voltage, power, efficiency, input admittance, and the radial distributions of displacement and stress. The effects of the load impedance and driving frequency are examined.

1. Introduction

There has been recent interest in periodically recharging batteries to power electronic devices operating in a sealed armor or other hazardous environments into which the physical access is prohibited. For instance, to ensure the reliability and performance of nuclear stockpiles, there have been proposals that piezoelectric transducers are used to generate acoustic waves propagating through a sealed armor for transmitting a small amount of power to the electronic devices inside the armor. The possibility of transmitting a certain amount of energy through an elastic wall was explored by theoretical and experimental studies in some recent articles [1–9]. The procedure involves the generation and propagation of acoustic waves, and energy harvesting from the waves using piezoelectric transducers. Once the acoustic wave energy is harvested into electrical energy, batteries can be charged through circuit design [10–13]. The feasibility of this power transmission technique was demonstrated experimentally with 110 W power at 88% efficiency [4].

For plate piezoelectric transducers, electromechanical energy conversion can be achieved through thickness-stretch vibrations or torsional vibrations [14]. As for cylindrical piezoelectric transducers, the conversion is attainable through axial thickness-shear motion with axial poling and radial electric fields [15], or through radial and circumferential expansion with circumferential poling [16]. Kim and Lee [17] investigate the radial vibration of a single-layered piezoelectric cylindrical transducer with radial poling. They obtained analytical results in terms of Bessel functions and verified the results using finite element analysis. Bessel functions were also used by Lin [18] to study the radial vibration characteristics of a cylindrical ring with an inner metal layer and an outer piezoelectric ceramic layer poled in the radial

* Corresponding author at: Department of Civil Engineering, Zhejiang University, Hangzhou 310058, PR China. Tel.: +86 571 87986672; fax: +86 571 87952165.
E-mail address: chenwq@zju.edu.cn (W.Q. Chen).

0022-460X/$ - see front matter © 2009 Elsevier Ltd. All rights reserved.
doi:10.1016/j.jsv.2009.04.002

Nomenclature

a, b, c, d	radii of the cylinder
c_{ij}	elastic constants
D_r	radial electric displacement
e_{ij}	piezoelectric constants
ε_{11}	dielectric constant
E	Young's modulus
φ	electric potential
η	transmission efficiency
I_1, I_2	input and output currents
k	wavenumber
v	Poisson's ratio
P_1, P_2	input and output powers
Q_1, Q_2	input and output charges
r	radial coordinate
ρ	mass density
T_r, T_θ	radial and circumferential normal stresses
u_r	radial displacement
v	wave speed
V_1, V_2	input and output voltages
ω	circular frequency
Z	load impedance

direction. In his work, the relations among the resonance frequency, the anti-resonance frequency, the effective electromechanical coupling coefficient, and the geometrical dimensions were investigated. The numerical results were validated by comparison with finite element method and experimental results.

Recently, Yang et al. [8,9] reported theoretical analyses on the electric energy transmission through a hollow cylinder with piezoelectric rings [8] or finite patches [9] on the inner and outer surfaces. The piezoelectric layers were poled in the axial direction, and the structures were driven into thickness-shear vibrations. A natural variation of the structure in Refs. [8,9] is to use radially polarized circular cylindrical ceramic transducers to excite thickness-stretch modes. The axially poled cylindrical shells in Refs. [8,9] require different electrodes for poling and operating. To create axial poling in a circular cylindrical shell, a relatively high voltage is needed between the two end faces of the shell. In comparison, radially polarized cylindrical ceramic shells use the same electrodes for poling and operating [17,18], and a relatively low voltage across the relatively small shell thickness is needed for poling. Therefore, radially polarized ceramic shell transducers have advantages in their manufacturing.

In this paper, it is proposed to use circular cylindrical ceramic transducers with radial polarization for power transmission through an elastic wall. In this configuration, under the driving electric field in the radial direction, thickness-stretch motion is produced through e_{11}. One advantage of this structure and material orientation is that the same electrodes used in poling the material can also be used for device operation. An exact solution from the linear theory of piezoelasticity [19] is obtained in the form of Bessel functions. The solution is validated by comparing numerical results to those obtained using the well-established state space method (SSM) [19–21] based on the theory of piezoelasticity. Various quantities of basic design interest such as output voltage and current, input admittance, efficiency, and mechanical fields are calculated and their dependence on the driving frequency and load impedance is examined.

2. Basic equations

Consider a three-layered, hollow cylinder whose cross-section is shown in Fig. 1. The middle layer ($b \leqslant r \leqslant c$) represents an elastic wall which is made of some isotropic metal. The inner layer ($a \leqslant r \leqslant b$) and the outer layer ($c \leqslant r \leqslant d$) are piezoelectric transducers made of ceramics poled in the radial direction. Any two adjacent layers are assumed perfectly bonded to each other.

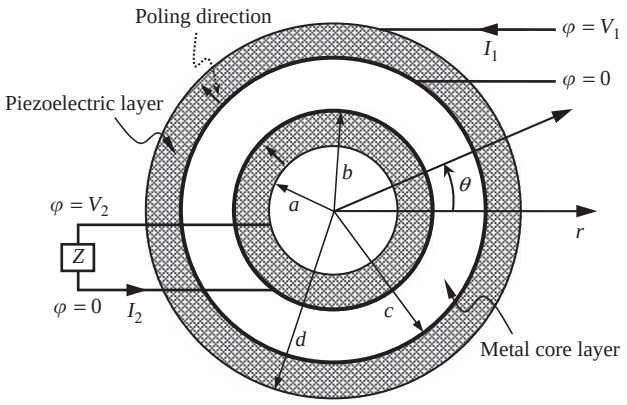

Fig. 1. Sketch of a power transmission system composed of piezoelectric hollow cylinder.

The x_3 axis is determined from the x_1 and x_2 axes by the right-hand rule. The cylinder is infinite in the x_3 direction. A cylindrical coordinate system is defined such that $x_1 = r\cos\theta$, $x_2 = r\sin\theta$, and $x_3 = z$. The unit vectors of the polar coordinate system $\{\mathbf{e}_r, \mathbf{e}_\theta, \mathbf{e}_z\}$ are ordered as $\{\mathbf{e}_1, \mathbf{e}_2, \mathbf{e}_3\}$ so that the radial poling is locally along $\mathbf{e}_1$. The inner and outer faces of the composite shell at $r = a$ and d are traction-free. The surfaces of the piezoelectric layers at $r = a$, b, c and d are all electroded. The elastic metal wall is grounded as a reference for the electric potential. A prescribed, driving voltage V_1 is applied across the electrodes at $r = c$ and d. Due to the particular material orientation, the shell is driven into radial or thickness-stretch vibration, and an output voltage V_2 can be picked up across the electrodes at $r = a$ and b, which are joined by a load circuit whose impedance is Z in time-harmonic motions. The structure is in plane-strain motions with $u_z = u_3 = 0$ and $\partial/\partial z = 0$. For an infinite cylinder the plane strain motion is exact. In real applications, when the length of a cylinder is much larger than its radial dimension, the end effects in the cylinder can be neglected and the problem is approximately plane-strain. For cylinders that are not very long, the end effects need to be considered and it becomes a much more challenging problem. In addition to the plain-strain motions, we have axisymmetry with $u_\theta = u_2 = 0$ and $\partial/\partial\theta = 0$. In this case, for the piezoelectric layers, the nonzero stress and electric displacement components are given by the following constitutive relations [19]:

$$T_r = T_1 = c_{11}\frac{\partial u_r}{\partial r} + c_{12}\frac{u_r}{r} + e_{11}\frac{\partial \varphi}{\partial r},$$

$$T_\theta = T_2 = c_{12}\frac{\partial u_r}{\partial r} + c_{22}\frac{u_r}{r} + e_{12}\frac{\partial \varphi}{\partial r},$$

$$D_r = D_1 = e_{11}\frac{\partial u_r}{\partial r} + e_{12}\frac{u_r}{r} - \varepsilon_{11}\frac{\partial \varphi}{\partial r}, \tag{1}$$

where $u_r = u_1 = u_r(r,t)$. The relevant equations of motion and the charge equation of electrostatics (Gauss) are

$$\frac{\partial T_r}{\partial r} + \frac{1}{r}(T_r - T_\theta) = \rho\frac{\partial^2 u_r}{\partial t^2}, \tag{2}$$

$$\frac{1}{r}\frac{\partial}{\partial r}(rD_r) = 0. \tag{3}$$

Eq. (3) can be integrated to give

$$D_r = \frac{A_3}{r}, \tag{4}$$

where A_3 is an integral constant.

For the isotropic elastic shell, the equation of motion is the same as Eq. (2) and the constitutive relations can be obtained from the first two of Eq. (1) by setting the piezoelectric constants to zero. For isotropic materials, c_{ij} in Eq. (1) can be determined by the Young's modulus E and the Poisson's ratio ν according to the following relations:

$$c_{\mathrm{m}11} = c_{\mathrm{m}22} = \frac{E(1-\nu)}{(1+\nu)(1-2\nu)}, \quad c_{\mathrm{m}12} = \frac{E\nu}{(1+\nu)(1-2\nu)}. \tag{5}$$

To obtain the input and output powers, it is necessary to determine the charges and currents on the electrodes. Consider a unit length in the x_3 direction. For the input electrode at $r = d$, the charge and current are

$$Q_1 = \int_0^{2\pi} (-D_r|_{r=d}\, d)\, \mathrm{d}\theta,$$

$$I_1 = \dot{Q}_1, \tag{6}$$

where a superimposed dot represents the derivative with respective to time t. Similarly, for the output electrode at $r = a$, the charge and current are

$$Q_2 = \int_0^{2\pi} |D_r|_{r=a}\, a\, \mathrm{d}\theta,$$

$$I_2 = -\dot{Q}_2. \tag{7}$$

For harmonic motions with a driving circular frequency ω, we use the usual complex notation:

$$(u_r, \varphi, \sigma_r, D_r, V_1, I_1, Q_1, V_2, I_2, Q_2) = \mathrm{Re}\{(\bar{u}_r, \bar{\varphi}, \bar{\sigma}_r, \bar{D}_r, \bar{V}_1, \bar{I}_1, \bar{Q}_1, \bar{V}_2, \bar{I}_2, \bar{Q}_2)\exp(i\omega t)\}, \tag{8}$$

where $\mathrm{i} = \sqrt{-1}$ is the imaginary unit. Substituting Eq. (4) into Eqs. (6) and (7) results in

$$\bar{I}_1 = -\mathrm{i}2\pi\omega A_3^{(3)}, \quad \bar{I}_2 = -\mathrm{i}2\pi\omega A_3^{(1)}, \tag{9}$$

where, to distinguish quantities of different layers, the superscripts (1), (2) and (3) are used for the inner, middle and outer layers, respectively. For the output circuit, we have the following equation:

$$\bar{V}_2 = \bar{I}_2 Z. \tag{10}$$

Then, the input and output powers are given by

$$\begin{aligned} P_1 &= \tfrac{1}{4}(\bar{I}_1\bar{V}_1^* + \bar{I}_1^*\bar{V}_1), \\ P_2 &= \tfrac{1}{4}(\bar{I}_2\bar{V}_2^* + \bar{I}_2^*\bar{V}_2) = \tfrac{1}{4}(\bar{I}_2\bar{I}_2^* Z^* + \bar{I}_2^*\bar{I}_2 Z) = \tfrac{1}{4}\bar{I}_2\bar{I}_2^*(Z^* + Z) = \tfrac{1}{2}|\bar{I}_2|^2 \mathrm{Re}\{Z\}, \end{aligned} \tag{11}$$

where an asterisk represents complex conjugate. Consequently, the transmission efficiency is defined as

$$\eta = \frac{P_2}{P_1}. \tag{12}$$

3. Exact solution

Substituting Eq. (4) into the third of Eq. (1) gives

$$\frac{\partial\varphi}{\partial r} = \frac{e_{12}}{\varepsilon_{11}}\frac{u_r}{r} + \frac{e_{11}}{\varepsilon_{11}}\frac{\partial u_r}{\partial r} - \frac{A_3}{\varepsilon_{11}}\frac{1}{r}, \tag{13}$$

with which the stress components in Eq. (1) can be written as

$$\begin{aligned} T_r &= c_1\frac{\partial u_r}{\partial r} + c_2\frac{u_r}{r} - \frac{e_{11}}{\varepsilon_{11}}\frac{A_3}{r}, \\ T_\theta &= c_2\frac{\partial u_r}{\partial r} + c_3\frac{u_r}{r} - \frac{e_{12}}{\varepsilon_{11}}\frac{A_3}{r}, \end{aligned} \tag{14}$$

where $c_1 = c_{11} + e_{11}^2/\varepsilon_{11}$, $c_2 = c_{12} + e_{12}e_{11}/\varepsilon_{11}$, and $c_3 = c_{22} + e_{12}^2/\varepsilon_{11}$. Substitution of Eq. (14) into Eq. (2) leads to

$$\frac{\partial^2\bar{u}_r}{\partial r^2} + \frac{1}{r}\frac{\partial\bar{u}_r}{\partial r} + \left(k^2 - \frac{\alpha^2}{r^2}\right)\bar{u}_r = -\frac{e_{12}}{c_1\varepsilon_{11}}\frac{A_3}{r^2}, \quad (a\leqslant r\leqslant b,\ c\leqslant r\leqslant d), \tag{15}$$

for the piezoelectric layers, and

$$\frac{\partial^2\bar{u}_r}{\partial r^2} + \frac{1}{r}\frac{\partial\bar{u}_r}{\partial r} + \left(k_\mathrm{m}^2 - \frac{1}{r^2}\right)\bar{u}_r = 0, \quad (b\leqslant r\leqslant c), \tag{16}$$

for the elastic layer. In Eqs. (15) and (16) we have introduced $\alpha^2 = c_3/c_1$, $k = \omega/v$, and $v = \sqrt{c_1/\rho}$ for the piezoelectric layers, as well as $k_\mathrm{m} = \omega/v_\mathrm{m}$ and $v_\mathrm{m} = \sqrt{c_{\mathrm{m}11}/\rho_\mathrm{m}}$ for the elastic metal layer.

Eqs. (15) and (16) are, respectively, inhomogeneous and homogeneous Bessel's equations. The general solutions are

$$\bar{u}_r^{(i)} = A_1^{(i)}J_\alpha(kr) + A_2^{(i)}Y_\alpha(kr) + \bar{u}_p^{(i)}(r), \quad (i = 1,3) \tag{17}$$

$$\bar{u}_r^{(2)} = A_1^{(2)}J_1(k_\mathrm{m}r) + A_2^{(2)}Y_1(k_\mathrm{m}r) \tag{18}$$

where J_α and Y_α are Bessel functions of the first and second kinds, respectively, $A_1^{(i)}$ and $A_2^{(i)}$ $(i = 1,2,3)$ are undetermined constants, and $\bar{u}_p$ is the particular solution for the piezoelectric layers given by

$$\bar{u}_p^{(i)} = -A_3^{(i)}\frac{\pi}{2}\frac{e_{12}}{c_1\varepsilon_{11}}\left[J_\alpha(kr)\int_0^r\frac{Y_\alpha(k\xi)}{\xi}\,d\xi - Y_\alpha(kr)\int_0^r\frac{J_\alpha(k\xi)}{\xi}\,d\xi\right] \equiv -A_3^{(i)}\frac{e_{12}}{c_1\varepsilon_{11}}s_{-1,\alpha}(kr), \tag{19}$$

where $s_{\mu,\alpha}(x)$ is the Lommel function [22]. In obtaining Eq. (19), the following identity has been used:

$$J_\alpha(kr)Y'_\alpha(kr) - J'_\alpha(kr)Y_\alpha(kr) = \frac{2}{\pi r}, \tag{20}$$

in which a prime denotes differentiation with respect to r. The radial stress components in different layers will be needed in the boundary and continuity conditions. They can be obtained from Eq. (14) as

$$\begin{aligned} \bar{T}_r^{(i)} &= A_1^{(i)}\left[c_1J'_\alpha(kr) + c_2\frac{1}{r}J_\alpha(kr)\right] + A_2^{(i)}\left[c_1Y'_\alpha(kr) + c_2\frac{1}{r}Y_\alpha(kr)\right] \\ &\quad -A_3^{(i)}\left\{\frac{e_{12}}{c_1\varepsilon_{11}}\left[c_1s'_{-1,\alpha}(kr) + c_2\frac{1}{r}s_{-1,\alpha}(kr)\right] + \frac{e_{11}}{\varepsilon_{11}}\frac{1}{r}\right\}, \end{aligned} \tag{21}$$

for the surface piezoelectric layers ($i = 1, 3$), and

$$\bar{T}_r^{(2)} = A_1^{(2)}\left[c_{m11}J_1'(k_m r) + c_{m12}\frac{1}{r}J_1(k_m r)\right] + A_2^{(2)}\left[c_{m11}Y_1'(k_m r) + c_{m12}\frac{1}{r}Y_1(k_m r)\right] \tag{22}$$

for the elastic layer. The expressions for the electric potentials in the piezoelectric layers can be obtained by integrating Eq. (13)

$$\bar{\varphi} = A_1^{(i)}\left[\frac{e_{12}}{\varepsilon_{11}}\int_0^r \frac{J_\alpha(k\xi)}{\xi}\,d\xi + \frac{e_{11}}{\varepsilon_{11}}J_\alpha(kr)\right] + A_2^{(i)}\left[\frac{e_{12}}{\varepsilon_{11}}\int_0^r \frac{Y_\alpha(k\xi)}{\xi}\,d\xi + \frac{e_{11}}{\varepsilon_{11}}Y_\alpha(kr)\right]$$

$$-A_3^{(i)}\left\{\frac{e_{12}}{c_1\varepsilon_{11}}\left[\frac{e_{12}}{\varepsilon_{11}}\int_0^r \frac{s_{-1,\alpha}(k\xi)}{\xi}\,d\xi + \frac{e_{11}}{\varepsilon_{11}}s_{-1,\alpha}(kr)\right] + \frac{1}{\varepsilon_{11}}\ln r\right\} + A_4^{(i)}, \tag{23}$$

where $i = 1, 3$. $A_4^{(i)}$ is another integration constant. There are totally ten constants, $A_1^{(i)}$, $A_2^{(i)}$, $A_3^{(i)}$ and $A_4^{(i)}(i = 1, 3)$, and $A_1^{(2)}$ and $A_2^{(2)}$, to be determined from the boundary and continuity conditions.

The boundary conditions for mechanical field at the inner and outer surfaces are

$$\bar{T}_r^{(1)}(a) = \bar{T}_r^{(3)}(d) = 0, \tag{24}$$

$$\bar{\varphi}^{(1)}(a) = \bar{V}_2 = -i2\pi\omega A_3^{(1)}Z, \quad \bar{\varphi}^{(3)}(d) = \bar{V}_1, \tag{25}$$

and that for electric field at the interfaces are

$$\bar{\varphi}^{(1)}(b) = \bar{\varphi}^{(3)}(c) = 0. \tag{26}$$

The continuity conditions for mechanical field at the interfaces are

$$\bar{T}_r^{(1)}(b) = \bar{T}_r^{(2)}(b), \quad \bar{u}_r^{(1)}(b) = \bar{u}_r^{(2)}(b), \tag{27}$$

$$\bar{T}_r^{(2)}(c) = \bar{T}_r^{(3)}(c), \quad \bar{u}_r^{(2)}(c) = \bar{u}_r^{(3)}(c). \tag{28}$$

Substituting Eqs. (17) and (21)–(23) into Eqs. (24)–(28) results in a system of inhomogeneous, linear algebraic equations for the ten unknown constants.

4. Numerical results

As an example, we consider PZT-5H for the polarized ceramics [8]. The relevant material constants are taken from Ref. [23]: $c_{11} = 117$ GPa, $c_{22} = 126$ GPa, $c_{12} = 8.14$ GPa, $e_{12} = -6.5$ C/m^2, $e_{11} = 23.3$ C/m^2, $\varepsilon_{11} = 1.302 \times 10^{-8}$ C/Vm, and $\rho = 7500$ kg/m^3. For the elastic layer, we consider iron with $E = 210$ GPa, $\nu = 0.25$, and $\rho = 7800$ kg/m^3 [8]. Damping is introduced by allowing the relevant elastic constants of the piezoelectric layers to assume complex values, which can represent viscous damping in the material. In our calculations, c_{11} is replaced by $c_{11}(1+iQ^{-1})$ where Q is a large and real number. The rest of

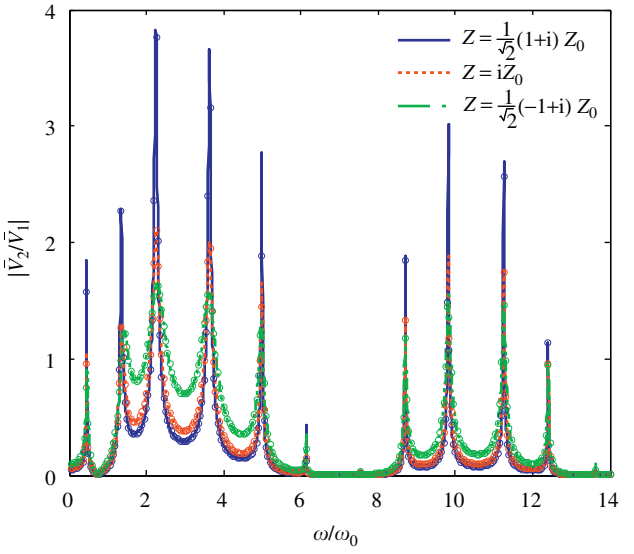

Fig. 2. Output voltage versus driving frequency for different loads. Present solution: lines. SSM: circles.

the elastic constants of the piezoelectric layers are treated similarly. For polarized ceramics, the value of Q is of the order of 10^2 to 10^3. Here, $Q = 10^3$ is used in the calculation. The geometric dimensions are $a = 10\,\text{mm}$, $b = 20\,\text{mm}$, $c = 30\,\text{mm}$, and $d = 40\,\text{mm}$. The following reference frequency and reference load impedance are used as the units for the driving frequency and the applied load impedance:

$$\omega_0^2 = \frac{\pi^2 c_{11}}{\rho(d-a)^2}, \quad Z_0 = \frac{1}{\mathrm{i}\omega C_0}, \quad C_0 = \frac{\varepsilon_{11} 2\pi}{\ln(b/a)}, \tag{29}$$

where ω_0 is related to the fundamental thickness-stretch frequency of the shell when $a \to \infty$, and C_0 is the static capacitance of the output transducer. In calculating ω_0, c_{11} is kept real. It should be pointed out that when the material constants are complex, α, the order of the Bessel functions, also becomes complex. This causes considerable complication in numerical calculation. Since the imaginary parts of the complex material constants are much smaller than the real parts, in the calculation of α only, we ignore the imaginary part of α. It will be shown later by comparison with the SSM that the error due to treating α as a real number is very small. The formulation using the SSM for the present axisymmetric deformation of hollow cylinders is given in the appendix where no approximation of dropping the imaginary part of a complex number is needed.

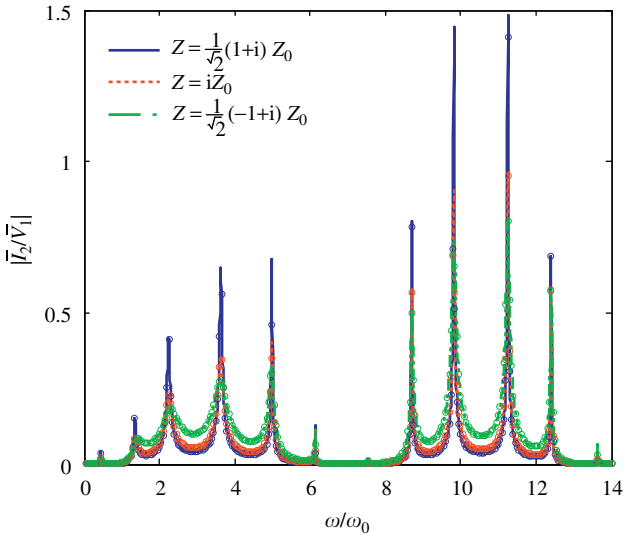

Fig. 3. Output admittance (in $1/\Omega$) versus driving frequency for different loads. Present solution: lines. SSM: circles.

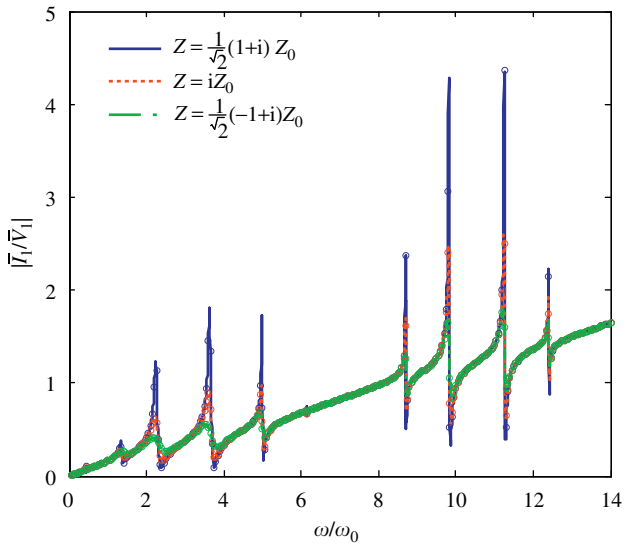

Fig. 4. Input admittance (in $1/\Omega$) versus driving frequency for different loads. Present solution: lines. SSM: circles.

Figs. 2–4 show, respectively, the normalized output voltage $|\bar{V}_2|/|\bar{V}_1|$, output current $|\bar{I}_2|/|\bar{V}_1|$ (in $1/\Omega$), and input admittance $|\bar{I}_1|/|\bar{V}_1|$ (in $1/\Omega$) versus the driving frequency ω. Three different loads are considered, i.e., $Z=\frac{1}{\sqrt{2}}(1+\mathrm{i})Z_0$, $Z=\mathrm{i}Z_0$, and $Z=\frac{1}{\sqrt{2}}(-1+\mathrm{i})Z_0$. The second load is a real number representing a pure resistor. The results from the SSM are also shown in the figures by circular markers for comparison. The two solutions agree very well. This shows that the error due to treating α as a real number is indeed very small.

Figs. 2 and 3 show that the output voltage and current attain maxima at resonant frequencies. This indicates that effective power transmission can happen at resonant frequencies. The global maximal output voltage in the present structure is about 3.8 times the input voltage. The frequency at which the input admittance assumes minimum is called the anti-resonant frequency. Unlike the situation of using thickness-shear modes for power transmission [8] wherein the output voltage attains its global maximum at the first resonance, in the present thickness-stretch mode structure the global maximum of the output voltage occurs at the third resonance (Fig. 2). In contrast, the global maximum of the output current occurs at a much higher resonance as shown in Fig. 3. Fig. 2 also shows that, among the three loads plotted, when $Z=\frac{1}{\sqrt{2}}(1+\mathrm{i})Z_0$ the output voltage is the largest, and when $Z=\frac{1}{\sqrt{2}}(-1+\mathrm{i})Z_0$ the output voltage is the smallest. The output current and the input admittance are similar. Note in Figs. 2–4 that the resonant frequencies in fact depend on the load impedance Z. However, this dependence is not strong and cannot be seen in the figures.

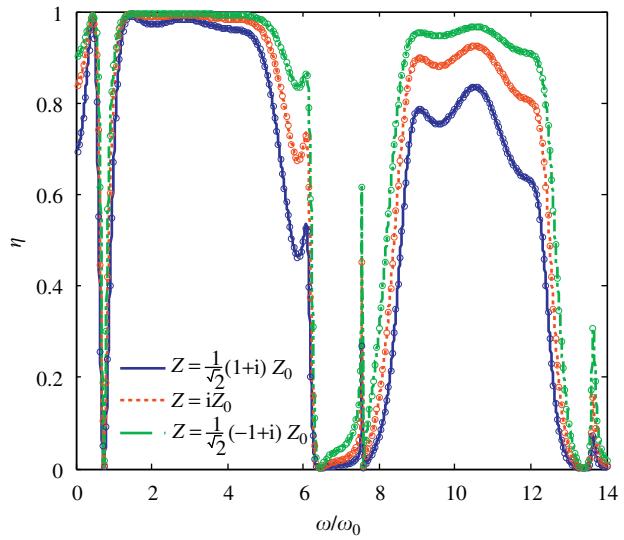

Fig. 5. Efficiency versus driving frequency for different loads. Present solution: lines. SSM: circles.

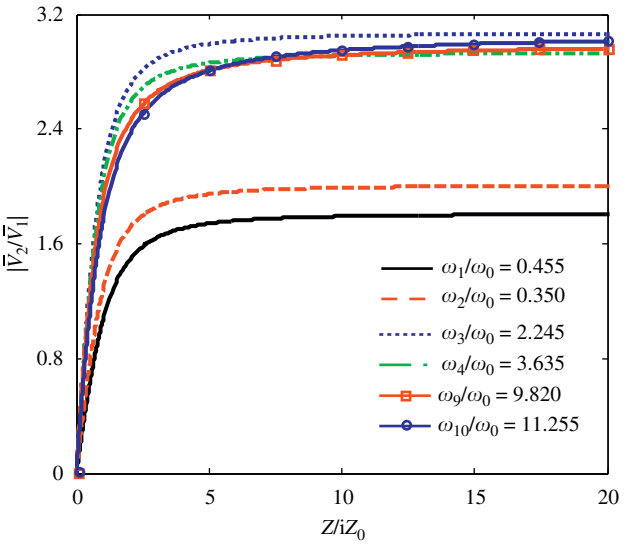

Fig. 6. Output voltage versus load near different resonant frequencies.

Fig. 5 shows the transmission efficiency η versus the driving frequency. Again, the results by ignoring the imaginary part of α are essentially identical to that from the SSM with complete complex elastic constants. Since both the output and input powers are functions of the driving frequency with sharp peaks, their ratio (efficiency) exhibits a rather complicated frequency behavior. The efficiency is bounded from above by 1. Among the three loads considered, the efficiency when $Z=\frac{1}{\sqrt{2}}(-1+\mathrm{i})Z_0$ is higher than that when $Z=\frac{1}{\sqrt{2}}(1+\mathrm{i})Z_0$. The efficiency is nearly zero when the normalized frequency equals 0.74. Similar behavior is observed when the normalized frequency equals 6.4, 7.6 and 13.4. These frequencies should be avoided in operation. We note that the efficiency shown in Fig. 5 is higher than the electromechanical coupling coefficient for polarized ceramics which is defined for static processes and is usually about 70–80%. In resonant piezoelectric devices like piezoelectric transformers in time-harmonic motions the energy conversion rate is often higher than the electromechanical coupling coefficient. This high efficiency can only be achieved for a certain range of the load Z.

Fig. 6–8 present $|\bar{V}_2|/|\bar{V}_1|$, $|\bar{I}_2|/|\bar{V}_1|$ and $|\bar{I}_1|/|\bar{V}_1|$ versus the normalized load $Z/\mathrm{i}Z_0$ for frequencies near different resonances. For these three figures, the load Z is taken as a real number and represents a pure resistor. In the figures ω_i represents the case when the driving frequency ω is very close to the ith resonance. The output voltage increases from zero drastically almost in a linear manner (Fig. 6) while the output current decreases sharply (Fig. 7) as the load increases from zero. For large loads, the output voltage and the input admittance are nearly constant, indicating saturation. Physically, for

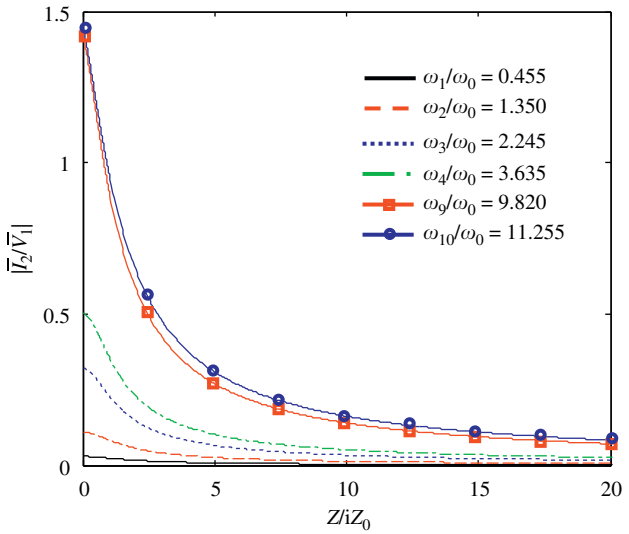

Fig. 7. Output admittance (in $1/\Omega$) versus load near different resonant frequencies.

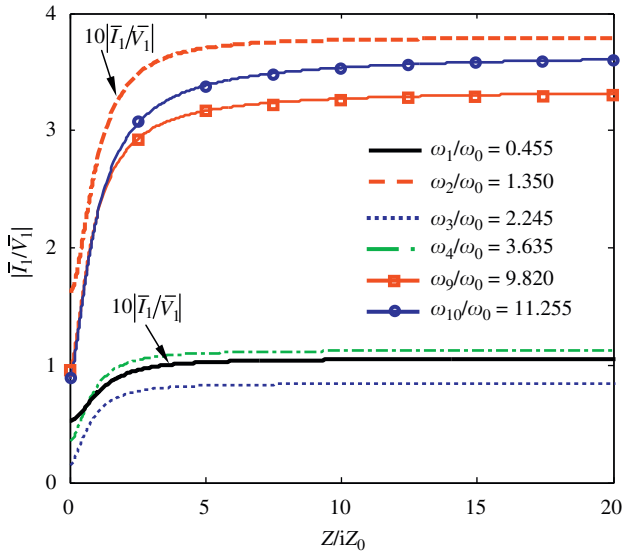

Fig. 8. Input admittance (in $1/\Omega$) versus load near different resonant frequencies.

very large loads, the output electrodes are essentially open, hence the output voltage is saturated and the output current nearly vanishes.

Efficiency versus load near resonant frequencies is plotted in Fig. 9. The efficiency first increases from zero to a maximum, and then decreases monotonically as $Z/\mathrm{i}Z_0$ increases (here Z is a real number). The efficiency near lower resonances (ω_1 to ω_4) is higher than that near higher resonances (ω_9 and ω_{10}). The presence of a maximal efficiency sets a clear goal for the optimization of structural design.

Finally, the radial distributions of $\bar{u}_r$ and $\bar{T}_r$ due to a unit input voltage ($|\bar{V}_1| = 1$) are shown in Figs. 10 and 11, respectively. The results are for $Z = \frac{1}{\sqrt{2}}(1+\mathrm{i})Z_0$, $Z = \mathrm{i}Z_0$ and $Z = \frac{1}{\sqrt{2}}(-1+\mathrm{i})Z_0$ near the first and third resonant frequencies, i.e. $\omega_1/\omega_0 = 0.455$ and $\omega_3/\omega_0 = 2.245$. The stresses near the first resonance are in kPa, and those near the third resonance in 10 kPa. The stress vanishes at the inner and outer surfaces of the cylinder as dictated by the traction-free boundary conditions in Eq. (24). Although these mechanical fields are not directly related to power transmission performance, they often need to be considered in design for structural strength. Among the loads considered, both the displacement and the stress attain maxima for $Z = \frac{1}{\sqrt{2}}(1+\mathrm{i})Z_0$ and minima for $Z = \frac{1}{\sqrt{2}}(-1+\mathrm{i})Z_0$. The displacements for all loads near the first resonance are larger than their counterparts near the third resonance. However, the trend for the stresses is the opposite.

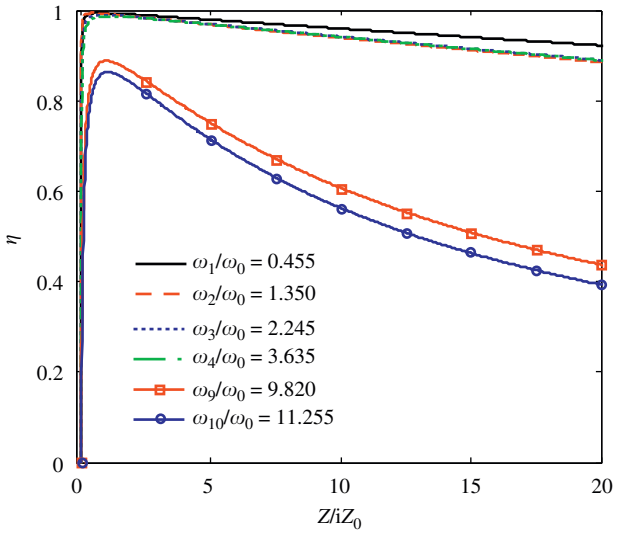

Fig. 9. Efficiency versus load near different resonant frequencies.

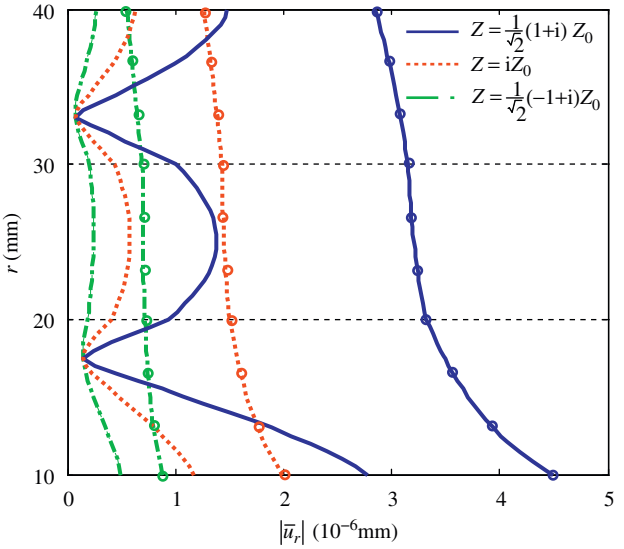

Fig. 10. Radial distribution of the displacement $|\bar{u}_r|$ for unit load with different phase angle. Lines with circular markers are for $\omega_1/\omega_0 = 0.455$. Others are for $\omega_3/\omega_0 = 2.245$.

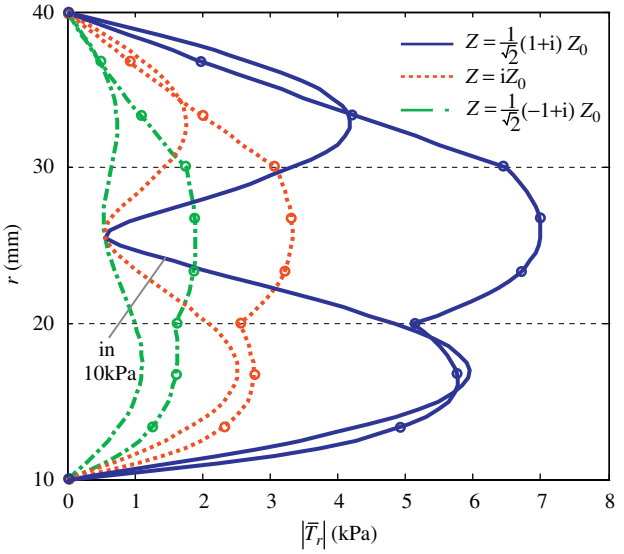

Fig. 11. Radial distribution of the normal stress $|\bar{T}_r|$ for unit load with different phase angle. Lines with circular markers are for $\omega_1/\omega_0 = 0.455$. Others are for $\omega_3/\omega_0 = 2.245$.

The maximal stress for the present example occurs within the armor for the first resonance and within the piezoelectric layers for the third resonance, rather than close to the interfaces. The location and magnitude of the maximal stress are shown clearly in Fig. 11, which are of importance in design.

5. Conclusion

An analysis was performed for transmission of energy by acoustic waves through an elastic hollow cylinder using piezoelectric ceramic transducers with radial poling. An exact solution in the form of Bessel functions was obtained and validated by comparison with the well-established SSM. Numerical examples were presented to investigate the output voltage and efficiency. It was found that effective power transmission can happen at a few lower-order resonant frequencies. For the example analyzed, the highest output voltage occurs at the third resonance. The efficiency can be very high, close to 1 over a frequency range including the first few resonances.

Acknowledgement

This research is supported by the National Natural Science Foundation of China (nos. 10725210, 10832009 and 10702061), and the Specialized Research Fund for the Doctoral Program of Higher Education (no. 20060335107). It was also supported by a grant from the Science and Technology Division, Zhejiang Province, China, under Key Technological Initiative Program (Project no. 2006C14021). Additional supports are from Ningbo University through the Qianjiang Fellow Fund and the Research Promotion Initiative.

Appendix A. State space analysis

The state space formulation for the piezoelectric layers is as follows:

$$\frac{\mathrm{d}}{\mathrm{d}r}\begin{Bmatrix}\bar{T}_r\\ \bar{u}_r\\ \bar{\varphi}\\ \bar{D}_r\end{Bmatrix}=\begin{bmatrix}\frac{1}{r}(a_1-1) & \frac{a_3}{r^2}-\rho\omega^2 & 0 & \frac{a_2}{r}\\ \frac{1}{c_1} & -\frac{a_1}{r} & 0 & \frac{e_{11}}{c_1\varepsilon_{11}}\\ \frac{e_{11}}{c_1\varepsilon_{11}} & -\frac{a_2}{r} & 0 & -\frac{c_{11}}{c_1\varepsilon_{11}}\\ 0 & 0 & 0 & -\frac{1}{r}\end{bmatrix}\begin{Bmatrix}\bar{T}_r\\ \bar{u}_r\\ \bar{\varphi}\\ \bar{D}_r\end{Bmatrix} \tag{A.1}$$

where $\bar{T}_r$, $\bar{u}_r$, $\bar{\varphi}$ and $\bar{D}_r$ are termed the state variables, and a_i $(i = 1,2,3)$ depend on material parameters and are defined by

$$a_1=\frac{c_2}{c_1},\quad a_2=\frac{e_{11}c_{12}-e_{12}c_{11}}{c_1\varepsilon_{11}},\quad a_3=c_{22}-c_{12}a_1-e_{12}a_2. \tag{A.2}$$

For the elastic shell, the state equation is obtained by discarding the electric quantities in Eq. (A.1), i.e.,

$$\frac{\mathrm{d}}{\mathrm{d}r}\begin{Bmatrix}\bar{T}_r\\ \bar{u}_r\end{Bmatrix}=\begin{bmatrix}\left(\dfrac{c_{\mathrm{m}12}}{c_{\mathrm{m}11}}-1\right)\dfrac{1}{r} & \left(c_{\mathrm{m}22}-\dfrac{c_{\mathrm{m}12}^2}{c_{\mathrm{m}11}}\right)\dfrac{1}{r^2}-\rho_{\mathrm{m}}\omega^2\\ \dfrac{1}{c_{\mathrm{m}11}} & -\dfrac{c_{\mathrm{m}12}}{c_{\mathrm{m}11}}\dfrac{1}{r}\end{bmatrix}\begin{Bmatrix}\bar{T}_r\\ \bar{u}_r\end{Bmatrix}. \tag{A.3}$$

Since Eqs. (A.1) and (A.3) have variable coefficients, the approximate laminate model [19–21] is adopted to divide the cylinder into many thin layers, for each layer the state equation approximately has constant coefficients. The general solution for each layer is readily obtained by solving the first-order differential equation. With the incorporation of mechanical continuity conditions and electric potential conditions at the interfaces, a transfer relation between the state vectors at the lateral surfaces where $r=a$ and $r=d$ is obtained. Based on this relation and the boundary conditions at lateral surfaces, the unknown state variables at the lateral surfaces are obtained, and, hence the global solution for the whole cylinder.

References

[1] Y.T. Hu, X. Zhang, J.S. Yang, et al., Transmitting electric energy through a metal wall by acoustic waves using piezoelectric transducers, *IEEE Transactions on Ultrasonics, Ferroelectrics, and Frequency Control* 50 (2003) 773–781.
[2] G.J. Saulnier, H.A. Scarton, A.J. Gavens, et al., Through-wall communication of low-rate digital data using ultrasound, *Proceedings of IEEE Ultrasonics Symposium*, British Columbia, Canada, 2006, pp. 1385–1389.
[3] T. Oishi, B. Aronov, D.A. Brown, Broadband multimode baffled piezoelectric cylindrical shell transducers, *Journal of the Acoustical Society of America* 121 (2007) 3465–3471.
[4] X.Q. Bao, B.J. Doty, S. Sherrit, et al., Wireless piezoelectric acoustic-electric power feedthru, *Proceeding of SPIE* (San Diego, USA), 2007, Vol. 6529, paper no. 652940.
[5] M. Ferrari, V. Ferrari, M. Guizzetti, et al., Piezoelectric multifrequency energy converter for power harvesting in autonomous microsystems, *Sensors and Actuators A—Physical* 142 (2008) 329–335.
[6] Z.T. Yang, J.S. Yang, Y.T. Hu, Energy trapping in power transmission through an elastic plate by finite piezoelectric transducers, *IEEE Transactions on Ultrasonics, Ferroelectrics, and Frequency Control* 55 (2008) 2493–2501.
[7] Z.T. Yang, J.S. Yang, Y.T. Hu, Nonlinear behavior of electric power transmission through an elastic wall by acoustic waves and piezoelectric transducers, *IEEE Transactions on Ultrasonics, Ferroelectrics, and Frequency Control* 55 (2008) 2527–2531.
[8] Z.T. Yang, S.H. Guo, J.S. Yang, Transmitting electric energy through a closed elastic wall by acoustic waves and piezoelectric transducers, *IEEE Transactions on Ultrasonics, Ferroelectrics, and Frequency Control* 55 (2008) 1380–1386.
[9] Z.T. Yang, S.H. Guo, Energy trapping in power transmission through a circular cylindrical elastic shell by finite piezoelectric transducers, *Ultrasonics* 48 (2008) 716–723.
[10] H.P. Hu, H. Xue, Y.T. Hu, A spiral-shaped harvester with an improved harvesting element and an adaptive storage circuit, *IEEE Transactions on Ultrasonics, Ferroelectrics, and Frequency Control* 54 (2007) 1177–1187.
[11] M.J. Guan, W.H. Liao, On the efficiencies of piezoelectric energy harvesting circuits towards storage device voltages, *Smart Materials and Structures* 16 (2007) 498–505.
[12] K. Nakano, S.J. Elliott, E. Rustighi, A unified approach to optimal conditions of power harvesting using electromagnetic and piezoelectric transducers, *Smart Materials and Structures* 16 (2007) 948–958.
[13] Y.T. Hu, T. Hu, Q. Jiang, On the interaction between the harvesting structure and the storage circuit of a piezoelectric energy harvester, *International Journal of Applied Electromagnetics and Mechanics* 27 (2008) 297–309.
[14] J.O. Kim, O.S. Kwon, Vibration characteristics of piezoelectric torsional transducers, *Journal of Sound and Vibration* 264 (2003) 453–473.
[15] I.J. Busch-Vishniac, *Electromechanical Sensors and Actuators*, Springer, New York, 1999 (Chapter 5).
[16] P. Lu, K.H. Lee, W.Z. Lin, et al., An approximate frequency formula for piezoelectric circular cylindrical shells, *Journal of Sound and Vibration* 242 (2001) 309–320.
[17] J.O. Kim, J.G. Lee, Dynamic characteristics of piezoelectric cylindrical transducers with radial polarization, *Journal of Sound and Vibration* 300 (2007) 241–249.
[18] S. Lin, Study on the radial vibration of a new type of composite piezoelectric transducer, *Journal of Sound and Vibration* 306 (2007) 192–202.
[19] H.J. Ding, W.Q. Chen, *Three Dimensional Problems of Piezoelasticity*, Nova Science Publishers, New York, 2001.
[20] W.Q. Chen, K.Y. Lee, Stresses in rotating cross-ply laminated hollow cylinders with arbitrary thickness, *Journal of Strain Analysis for Engineering Design* 39 (2004) 437–445.
[21] W.Q. Chen, Z.G. Bian, C.F. Lv, H.J. Ding, 3D free vibration analysis of a functionally graded piezoelectric hollow cylinder filled with compressible fluid, *International Journal of Solids and Structures* 41 (2004) 947–964.
[22] I.S. Gradshteyan, I.M. Ryzhik, *Table of Integrals, Series, and Products*, Academic Press, New York, 1980.
[23] H. Jaffe, D.A. Berlincourt, Piezoelectric transducer materials, *Proceedings of IEEE* 53 (1965) 1372–1386.